applied sciences

MDPI

Article

Hard Magnetic Properties of M-Type Sr-Hexaferrites via Ce–Mg Substitution and Ca-Assisted Solubility Enhancement

Do-Hwan Kim and Young-Min Kang *

Department of Materials Science and Engineering, Korea National University of Transportation, Chungju 27469, Republic of Korea; 2019006@a.ut.ac.kr
* Correspondence: ymkang@ut.ac.kr

Abstract

A cobalt-free compositional strategy was pursued to promote Ce incorporation in M-type $SrFe_{12}O_{19}$ and thereby enhance its hard magnetic performance. In $Sr_{1-x}Ce_xFe_{12-x}Mg_xO_{19}$ ($x = 0$–0.15), the highest coercivity and finest microstructure were obtained at $x = 0.1$; however, a residual CeO_2 phase persisted at all substitution levels, suggesting limited Ce incorporation. Partial replacement of Sr^{2+} by Ca^{2+} suppressed detectable CeO_2 reflections once $y \geq 0.2$ in $Sr_{0.9-y}Ca_yCe_{0.1}Fe_{11.9}Mg_{0.1}O_{19}$, providing indirect XRD evidence for enhanced Ce incorporation, although an α-Fe_2O_3 secondary phase remained. Reducing the nominal Fe content in $Sr_{0.7}Ca_{0.2}Ce_{0.1}Fe_{11.9-z}Mg_{0.1}O_{19}$ ($z = 0$–0.75) further suppressed the α-Fe_2O_3 reflections, which were no longer detected at $z = 0.75$ ($Sr_{0.7}Ca_{0.2}Ce_{0.1}Fe_{11.15}Mg_{0.1}O_{19}$). Because the Ca-containing compositions exhibited reduced coercivity, potentially associated with grain coarsening, high-energy milling combined with sintering-temperature and additive optimization (SiO_2, CaO, $SrCO_3$, Cr_2O_3, ZnO, Mn_2O_3) was applied to restore a fine growth-controlled microstructure, lifting coercivity from 2714 Oe to 3552–3911 Oe. Additive sets sharing a common SiO_2–CaO–$SrCO_3$ base with ZnO, Cr_2O_3, or Mn_2O_3 addition yielded a closely matched, favorable remanence–coercivity balance. This work demonstrates a cobalt-free composition–processing route to hard magnetic M-type hexaferrites through Ca-assisted Ce incorporation, nominal Fe-content adjustment, and microstructural control.

Keywords: M-type hexaferrite; permanent magnet; remanent magnetization; coercivity

1. Introduction

M-type hexaferrites, with the general formula $AFe_{12}O_{19}$ (A = Ba, Sr, or Pb), remain the most widely produced hard magnetic material, due to their high magnetocrystalline anisotropy, large coercivity (H_C), high Curie temperature, and excellent chemical and thermal stability [1–6]. Among the A-site variants, $SrFe_{12}O_{19}$ (SrM) is preferred over $BaFe_{12}O_{19}$ for most commercial permanent-magnet applications—motors, loudspeakers, and magnetic-recording media—because of its slightly higher magnetocrystalline anisotropy field and superior corrosion resistance. Nevertheless, the intrinsic saturation magnetization (M_S) and H_C of undoped SrM are no longer sufficient to satisfy the performance demands of high-efficiency BLDC motors, automotive traction motors, and energy-harvesting systems, all of which require magnets with simultaneously higher remanence and coercivity than conventional ferrite grades can offer.

To close this performance gap, Co^{2+} has traditionally been introduced together with rare-earth (RE) ions such as La^{3+} at the Sr site, since La–Co co-substitution is known to enhance the anisotropy field through spin–orbit coupling between Co^{2+} and Fe^{3+} [7–9].

Check for updates

Academic Editor: Roberto Zivieri

Received: 2 October 2026
Revised: 27 October 2026
Accepted: 27 October 2026
Published: 30 October 2026

Copyright: © 2026 by the authors. Licensee MDPI, Basel, Switzerland. This article is an open access article distributed under the terms and conditions of the Creative Commons Attribution (CC BY) license.

This La–Co strategy is currently the industrial standard for high-grade sintered ferrite magnets. However, Co is a critical and increasingly cost-volatile raw material subject to significant supply-chain risk, which has motivated an active search for Co-free alternatives capable of matching La–Co-level performance. Several groups have therefore explored RE substitution without Co. Grossinger et al. showed that La, Ce, and Nd substitution alone can enhance magnetocrystalline anisotropy and H_C through lattice distortion of the magnetoplumbite framework [10]. Lobo-Guerrero et al. confirmed in a recent review that La, Ce, Gd, and Sm substitution generally increases H_C and thermal stability while improving grain homogeneity in both BaM and SrM [11], and Todkar et al. demonstrated that Ce–Dy co-doping of BaM nanoparticles yields very high H_C, suitable even for microwave-absorber use [12]. Ce substitution in particular has been shown to enhance hard magnetic properties without Co: Ce–Mn co-substitution increased H_C from 4358 to 5050 Oe through enhanced crystalline anisotropy without a reduction in M_S [13], and La–Ce–Zn co-doping raised M_S to 76–78 emu/g—above the practical limit of undoped SrM—via oxygen-vacancy-assisted Fe^{3+}-to-Fe^{2+} reduction under controlled calcination atmosphere [14]. Oxygen potential has also been shown to influence Zn solubility and saturation magnetization in Co-free La–Zn-substituted SrM ferrites [15]. These results confirm Ce as an effective cobalt-free substituent for both M_S and H_C enhancement, motivating its selection as the RE dopant in the present study. Ce–Zn co-doping has also been investigated in BaM ferrites, revealing changes in crystal structure, microstructure, and magnetic behavior [16]. Divalent co-dopants such as Mg^{2+} have also been shown to refine grain morphology and, when paired with a RE ion, to produce a synergistic increase in both M_S and H_C without invoking Co—for example, La–Mg co-substituted SrM ($Sr_{0.9}La_{0.1}Fe_{11.9}Mg_{0.1}O_{19}$) was recently reported to reach M_S = 71.9 emu/g and H_C = 3549 Oe [17]. These results collectively establish RE–Mg co-substitution as a viable cobalt-free route to enhanced hard magnetic performance.

Among the candidate RE ions, Ce is particularly attractive because it is markedly more abundant and less expensive than La, Sm, or Gd, which makes it an economically preferable substituent for mass-produced ferrite magnets. However, Ce^{3+} has a larger ionic radius mismatch with Sr^{2+} at the 12-fold coordinated A-site than La^{3+}, and its solubility limit in the SrM lattice is correspondingly lower; when $Sr_{1-x}Ce_xFe_{12-x}Mg_xO_{19}$ is prepared by direct Ce-for-Sr substitution, only partial incorporation of Ce into the M-type lattice is achieved even at the composition ($x = 0.1$) that otherwise gives the most favorable magnetic properties, leaving residual non-hexaferrite Ce-related phases at the grain boundaries [18]. This incomplete solid solubility limits the amount of Ce that can be usefully substituted and, in turn, caps the anisotropy enhancement that RE substitution can deliver.

To overcome this solubility limitation, partial co-substitution of the A-site with Ca^{2+}—an ionic radius intermediate between Sr^{2+} and Ce^{3+}—was investigated as a means of relaxing the lattice strain associated with Ce incorporation. Introducing Ca^{2+} together with Ce^{3+} at the Sr-site was found to markedly improve the effective incorporation of Ce into the M-type structure, as indirectly supported by the disappearance of detectable CeO_2 reflections. However, XRD analysis of the nominal composition $Sr_{0.7}Ca_{0.2}Ce_{0.1}Fe_{11.9}Mg_{0.1}O_{19}$ still revealed α-Fe_2O_3 secondary-phase reflections. This observation motivated a systematic adjustment of the nominal Fe content to suppress these reflections while retaining the M-type structure, highlighting the importance of considering both A-site substitution and the nominal Fe content in multi-cation-substituted hexaferrites [19]. The beneficial role of Ca in substituted M-type ferrites has precedent in Ca–La–Co compositions, which exhibit higher magnetic anisotropy and improved magnet performance compared with Sr–La–Co ferrites [9,20]. This motivates the consideration of Ca as a means of modifying the structural environment and incorporation behavior of substituent cations. NMR and first-principles studies have also shown that the A-site cation influences Co site selectivity

in La–Co-substituted M-type ferrites [21]. In the present Co-free Ce–Mg system, however, the evidence concerns the suppression of detectable CeO_2 reflections; neither a Co-related anisotropy mechanism nor an equivalent performance enhancement is inferred. This study examines how Ca substitution, nominal Fe-content adjustment, and powder-processing control can be combined to address secondary-phase formation and the remanence–coercivity balance in the Co-free Ce–Mg system.

2. Materials and Methods

A series of M-type hexaferrites with the nominal compositions $Sr_{1-x}Ce_xFe_{12-x}Mg_xO_{19}$ (x = 0, 0.05, 0.1, 0.15), $Sr_{0.9-y}Ca_yCe_{0.1}Fe_{11.9}Mg_{0.1}O_{19}$ (y = 0, 0.1, 0.2, 0.3), and $Sr_{0.7}Ca_{0.2}Ce_{0.1}Fe_{11.9-z}Mg_{0.1}O_{19}$ (z = 0, 0.25, 0.5, 0.75) was prepared by a conventional solid-state reaction route. The formulas denote the nominal cation ratios used for batch preparation; the oxygen stoichiometry and actual composition of the M-type phase were not independently determined. High-purity Fe_2O_3 (99.5%, industrial grade), $SrCO_3$, CeO_2, $CaCO_3$, and MgO (the latter four powders: 99.9% purity, Kojundo Chemical Lab. Co., Ltd., Sakado, Japan) were weighed according to the nominal batch compositions. Each 50.00 g batch was loaded into a cylindrical polypropylene jar (7.2 cm in diameter and 17 cm in height) with 100 mL of deionized (DI) water and a mixture of yttria-stabilized ZrO_2 balls with 10, 5, and 3 mm diameters. The ball-to-powder mass ratio was 5:1, corresponding to approximately 250 g of balls per batch. The slurry was homogenized at 100 rpm for 24 h, oven-dried at 180 °C, and calcined in an alumina crucible in air for 4 h. The calcination temperature was 1100 °C for the three compositional series and 1080 °C for the selected composition used in the sintering-additive evaluation; the other initial preparation conditions were unchanged. After calcination, the powders for the three compositional series were crushed, sieved, and subjected to a second ZrO_2 ball-milling treatment at 100 rpm for 20 h using the same milling-media sizes and ball-to-powder mass ratio. For the three compositional series, 0.5 wt % SiO_2 and 1 wt % $CaCO_3$ were added during this second milling step.

For the sintering-additive evaluation, the selected nominal composition, $Sr_{0.7}Ca_{0.2}Ce_{0.1}Fe_{11.15}Mg_{0.1}O_{19}$, underwent an additional dry high-energy milling treatment before this final ZrO_2 milling step. A 25 g portion of the calcined powder was milled at 200 rpm for 2 h in a 500 mL steel jar (12.5 cm in diameter) with 500 g of 5 mm-diameter steel balls, giving a ball-to-powder mass ratio of 20:1. Milling durations of 1, 2, and 4 h were evaluated in preliminary trials, and 2 h was selected based on the magnetic properties of the resulting sintered specimens. The detailed optimization results are omitted for brevity. The powder was subsequently subjected to the same 20 h ZrO_2 ball-milling procedure described above. Sintering additives—SiO_2 (99.0%, industrial grade), CaO, Mn_2O_3, $SrCO_3$, Cr_2O_3, and ZnO (all 99.9% purity, Kojundo Chemical Lab. Co., Ltd., Sakado, Japan)—were introduced in different combinations during the final ZrO_2 ball-milling step. Each additive content was calculated relative to the mass of hexaferrite powder before additive addition; for example, 1 wt % denotes 1 g of additive per 100 g of hexaferrite powder. The resulting powders were oven-dried at 180 °C, uniaxially pressed into disk-shaped green compacts using a 30.0 mm-diameter mold at approximately 15 MPa, and sintered in air at 1210–1230 °C for 2 h. Heating and cooling rates of 5 and 8 °C min^{-1}, respectively, were used for all calcination and sintering treatments.

The bulk density of the sintered samples was determined from their weight and geometric dimensions. Phase identification was carried out by X-ray diffraction (XRD; D2 Phaser, Bruker AXS, Karlsruhe, Germany) using Cu-Kα radiation (λ = 0.15406 nm) over a 2θ range of 20–70°, with a step size of 0.0197° and a total scan time of 18 min per specimen. Microstructural features were examined by field-emission scanning electron microscopy (FE-SEM; JSM-7610F, JEOL Ltd., Akishima, Japan), and average grain sizes and grain-

size distributions were determined from SEM images using the line-intercept method, with approximately 200 grain intercepts evaluated per condition. Room-temperature magnetic hysteresis behavior was characterized using a vibrating-sample magnetometer (VSM; 7410, Lake Shore Cryotronics, Westerville, OH, USA) and a B–H loop tracer (BH-5501, Denshijiki Industry Co., Ltd., Tokyo, Japan). VSM measurements were performed on rectangular sintered specimens (~2.0 mm × 1.5 mm × 0.8 mm) under applied fields of −23 to 23 kOe, whereas B–H loop tracer measurements were conducted on disk-shaped specimens (~24 mm in diameter, ~6 mm thick) by sweeping the field from +20 kOe to −20 kOe to obtain the demagnetization curves. One specimen per condition was characterized by each measurement method.

3. Results and Discussion

Figure 1a shows the XRD patterns of $Sr_{1-x}Ce_xFe_{12-x}Mg_xO_{19}$ (x = 0–0.15). In the Ca-substituted series (Figure 1b), the CeO_2 reflection remains detectable at y = 0 and 0.1 but is no longer detected at y ≥ 0.2. This observation provides indirect XRD evidence that Ca substitution promotes Ce incorporation into the M-type phase under the present processing conditions. Although this interpretation is consistent with the suppression of crystalline CeO_2, the present measurements do not establish complete Ce incorporation, its oxidation state, or its crystallographic site occupancy. However, an α-Fe_2O_3 secondary phase is observed across the entire y = 0–0.3 range, indicating that the nominal Fe content exceeds what the lattice can accommodate once Ca and Ce jointly occupy the Sr-site. To eliminate this residual α-Fe_2O_3 phase, the Fe content was systematically reduced in $Sr_{0.7}Ca_{0.2}Ce_{0.1}Fe_{11.9-z}Mg_{0.1}O_{19}$ (z = 0–0.75) (Figure 1c). At z = 0.75, the diagnostic α-Fe_2O_3 reflection is no longer discernible under the present XRD conditions, although trace secondary phases cannot be excluded.

The lattice parameters (a, c) and unit-cell volume calculated from the XRD patterns in Figure 1a–c are summarized in Table 1. The lattice parameters were calculated from the measured (107) and (114) peak positions using Bragg's law and the hexagonal interplanar-spacing relation [22]. In the $Sr_{1-x}Ce_xFe_{12-x}Mg_xO_{19}$ series, a, c, and the cell volume vary irregularly with x (e.g., cell volume of 687.9 Å^3 at x = 0–0.05, a maximum of 689.4 Å^3 at x = 0.1, and a decrease to 686.7 Å^3 at x = 0.15), without a monotonic trend. In the $Sr_{0.9-y}Ca_yCe_{0.1}Fe_{11.9}Mg_{0.1}O_{19}$ series, the calculated cell volume increases from 689.0 Å^3 at y = 0–0.1 to 691.0 Å^3 at y = 0.2–0.3, accompanied by an increase in a from 5.878 to 5.886 Å, while c changes only slightly. This numerical change coincides with the disappearance of detectable CeO_2 reflections at y ≥ 0.2 (Figure 1b). However, the bounds reported in Table 1 represent angular-sampling contributions only, and the total experimental uncertainties in a, c, and the cell volume were not determined. These variations therefore do not independently establish lattice expansion or a specific incorporation mechanism. In the Fe-reduced series $Sr_{0.7}Ca_{0.2}Ce_{0.1}Fe_{11.9-z}Mg_{0.1}O_{19}$ (z = 0–0.75), the calculated lattice parameters and cell volume remain unchanged at the reported precision, while the α-Fe_2O_3 reflection intensity decreases (Figure 1c). Thus, reducing the nominal Fe content suppresses the detectable secondary-phase reflections without a resolved change in the calculated lattice parameters. The estimated angular-sampling contributions to the lattice-parameter bounds are approximately ±0.003 Å for a and ±0.015 Å for c. These estimates do not include systematic instrumental or specimen-related errors.

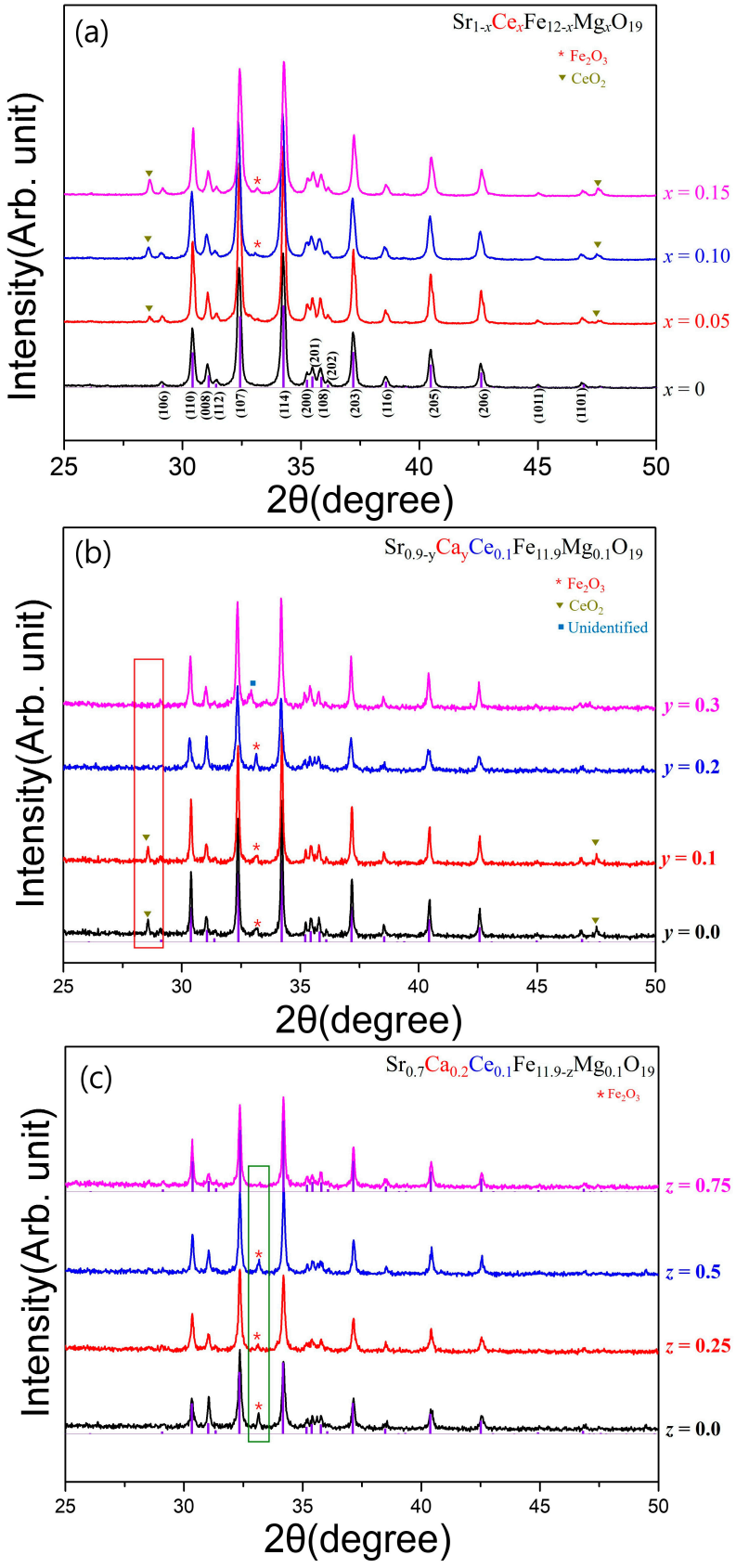


Figure 1. X-ray diffraction patterns of (**a**) $Sr_{1-x}Ce_xFe_{12-x}Mg_xO_{19}$ (x = 0, 0.05, 0.1, 0.15), (**b**) $Sr_{0.9-y}Ca_yCe_{0.1}Fe_{11.9}Mg_{0.1}O_{19}$ (y = 0, 0.1, 0.2, 0.3), and (**c**) $Sr_{0.7}Ca_{0.2}Ce_{0.1}Fe_{11.9-z}Mg_{0.1}O_{19}$ (z = 0, 0.25, 0.5, 0.75) powders after sintering at 1230 °C.

Table 1. Lattice parameters *a*, *c*, *c*/*a*, and cell volume of the M-type hexaferrites.

Composition	x, y, z	*a*	*c*	*c*/*a*	Cell Vol.
$Sr_{1-x}Ce_xFe_{12-x}Mg_xO_{19}$	x = 0	5.874	23.021	3.919	687.9
	x = 0.05	5.874	23.021	3.919	687.9
	x = 0.1	5.876	23.058	3.924	689.4
	x = 0.15	5.871	23.007	3.919	686.7
$Sr_{0.9-y}Ca_yCe_{0.1}Fe_{11.9}Mg_{0.1}O_{19}$	y = 0	5.878	23.028	3.918	689.0
	y = 0.1	5.878	23.028	3.918	689.0
	y = 0.2	5.886	23.035	3.914	691.0
	y = 0.3	5.886	23.035	3.914	691.0
$Sr_{0.7}Ca_{0.2}Ce_{0.1}Fe_{11.9-z}Mg_{0.1}O_{19}$	z = 0	5.886	23.035	3.914	691.0
	z = 0.25	5.886	23.035	3.914	691.0
	z = 0.5	5.886	23.035	3.914	691.0
	z = 0.75	5.886	23.035	3.914	691.0

Figure 2a–d shows the FE-SEM micrographs of $Sr_{1-x}Ce_xFe_{12-x}Mg_xO_{19}$ (x = 0, 0.05, 0.1, 0.15) sintered at 1230 °C, with the corresponding grain-size distributions in Figure 2e–h. The undoped sample (x = 0) exhibits a moderate average grain size of 1.45 μm with a relatively broad distribution extending up to ~4 μm. Upon introducing Ce–Mg co-substitution at x = 0.05, the average grain size increases to 1.62 μm, and the distribution broadens further, indicating that a small amount of Ce–Mg promotes grain growth, likely through enhanced mass transport at the grain boundaries or the presence of a Ce-rich secondary phase (cf. Figure 1a) acting as a local sintering aid. With a further increase to x = 0.1, the microstructure changes markedly: the average grain size drops sharply to 1.1 μm, the finest among the four compositions, and the distribution narrows and sharpens, with the majority of grains falling below 1.5 μm. The grain refinement at x = 0.1 may involve changes in grain-boundary mobility associated with the Ce–Mg substitution and secondary-phase formation. At x = 0.15, the average grain size increases slightly to 1.18 μm, remaining smaller than those at x = 0 and 0.05 but larger than that at x = 0.1. This non-monotonic variation suggests that the grain-growth response depends on the Ce–Mg substitution level, potentially through changes in phase formation and grain-boundary mobility. The inverse relationship between grain size and coercivity observed in Figures 2 and 3 can be interpreted qualitatively using the empirical relation for the relative coercivity (h_C) of individual crystal grains [23],

$$h_C = \frac{D_{cri}}{D_{ave}^{1.08}} \quad (1)$$

where D_{ave} is the average grain size, and D_{cri} is a material-specific critical grain diameter. This relation predicts that H_C increases monotonically as D decreases toward the single-domain regime, consistent with the finest grain structure at x = 0.1 (Figure 2c, D_{ave} = 1.1 μm) and coinciding with the maximum coercivity of the series (Figure 3b).

Figure 3a presents the room-temperature M–H curves of $Sr_{1-x}Ce_xFe_{12-x}Mg_xO_{19}$ (x = 0–0.15) measured by VSM on small (~0.1 g) specimens, with the corresponding M_S and H_C values plotted against x in Figure 3b. As x increases, M_S decreases monotonically from 69.71 emu/g (x = 0) to 66.11 emu/g (x = 0.15), which is attributed to the progressive increase in the non-magnetic CeO_2 secondary phase identified in the XRD patterns of Figure 1a: since only a limited fraction of the nominal Ce is incorporated into the M-type lattice, the remaining CeO_2 dilutes the magnetically active hexaferrite fraction and lowers the bulk magnetization. In contrast, H_C does not vary monotonically with x, reaching a clear maximum of 3343 Oe at x = 0.1 before decreasing again at x = 0.15. The highest measured coercivity at x = 0.1 coincides with the smallest measured average grain size, suggesting

that grain refinement contributes to the coercivity enhancement. However, contributions from magnetocrystalline anisotropy, defects, porosity, and intergranular phases cannot be separated using the present measurements. To verify these trends under application-relevant conditions, the same compositions were sintered into bulk disk-shaped samples (~24 mm in diameter) and measured by a B–H loop tracer (Figure 3c,d). The resulting $4\pi M_r$ and H_C values as a function of x follow essentially the same trend as the VSM results in Figure 3a,b—a general decline in $4\pi M_r$ with increasing x and a peak in H_C at x = 0.1 (3500 Oe)—confirming that the compositional dependence established on small VSM specimens is preserved at bulk scale. Based on these combined results, the Ce–Mg content was fixed at x = 0.1 for all subsequent compositional design.

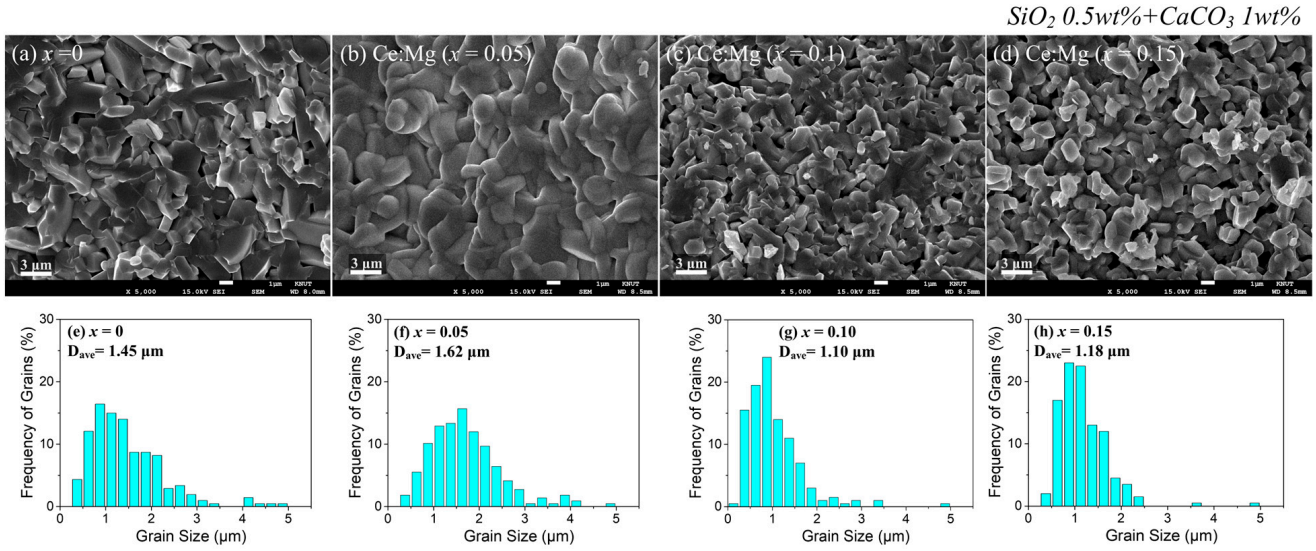


Figure 2. (**a**–**d**) SEM micrographs of $Sr_{1-x}Ce_xFe_{12-x}Mg_xO_{19}$ (x = 0, 0.05, 0.1, 0.15) samples sintered at 1230 °C and (**e**–**h**) grain size distribution histograms corresponding to the SEM micrographs of the samples shown in (**a**–**d**).

With x = 0.1 fixed, the A-site was further modified by Ca co-substitution. Figure 1b shows that the CeO_2 reflections were no longer detectable at y = 0.2 in $Sr_{0.9-y}Ca_yCe_{0.1}Fe_{11.9}Mg_{0.1}O_{19}$, corresponding to $Sr_{0.7}Ca_{0.2}Ce_{0.1}Fe_{11.9}Mg_{0.1}O_{19}$. However, this composition still contained a residual α-Fe_2O_3 secondary phase, whose diffraction intensity was suppressed by reducing the nominal Fe content in $Sr_{0.7}Ca_{0.2}Ce_{0.1}Fe_{11.9-z}Mg_{0.1}O_{19}$ (z = 0–0.75). The demagnetization curves and corresponding $4\pi M_r$ and H_C values for this Fe-reduced series are shown in Figure 3e,f. The quantitative data for the samples shown in Figure 3 are summarized in Table 2. As z increases from 0 to 0.75, $4\pi M_r$ increases overall from 2092 to 2385 G, despite non-monotonic intermediate values of 2277 G at z = 0.25 and 2046 G at z = 0.5. The higher remanence at z = 0.75 is consistent with the suppression of the α-Fe_2O_3 reflections in Figure 1c. Because the room-temperature magnetization of α-Fe_2O_3 is much smaller than that of the M-type ferrite, reducing its content is expected to lessen magnetic dilution and contribute to the remanence enhancement. This interpretation can be discussed qualitatively using the following relation for a polycrystalline ferrite magnet [14,17]:

$$4\pi M_r = 4\pi M_S \cdot \rho \cdot S \cdot (1 - f_i) \quad (2)$$

where ρ is the sintered density, S is the crystallographic orientation factor, and f_i represents the volume fraction of secondary phases whose magnetization is negligible relative to that of the M-type ferrite. An ideal randomly oriented assembly is represented by $S = 0.5$. The measured densities vary only slightly across the Fe-reduced series, whereas S and f_i were not

independently quantified. Equation (2) therefore provides a qualitative framework: the suppression of α-Fe_2O_3 is reasonably expected to contribute to the higher remanence at z = 0.75, although it does not quantitatively account for the non-monotonic intermediate variation.

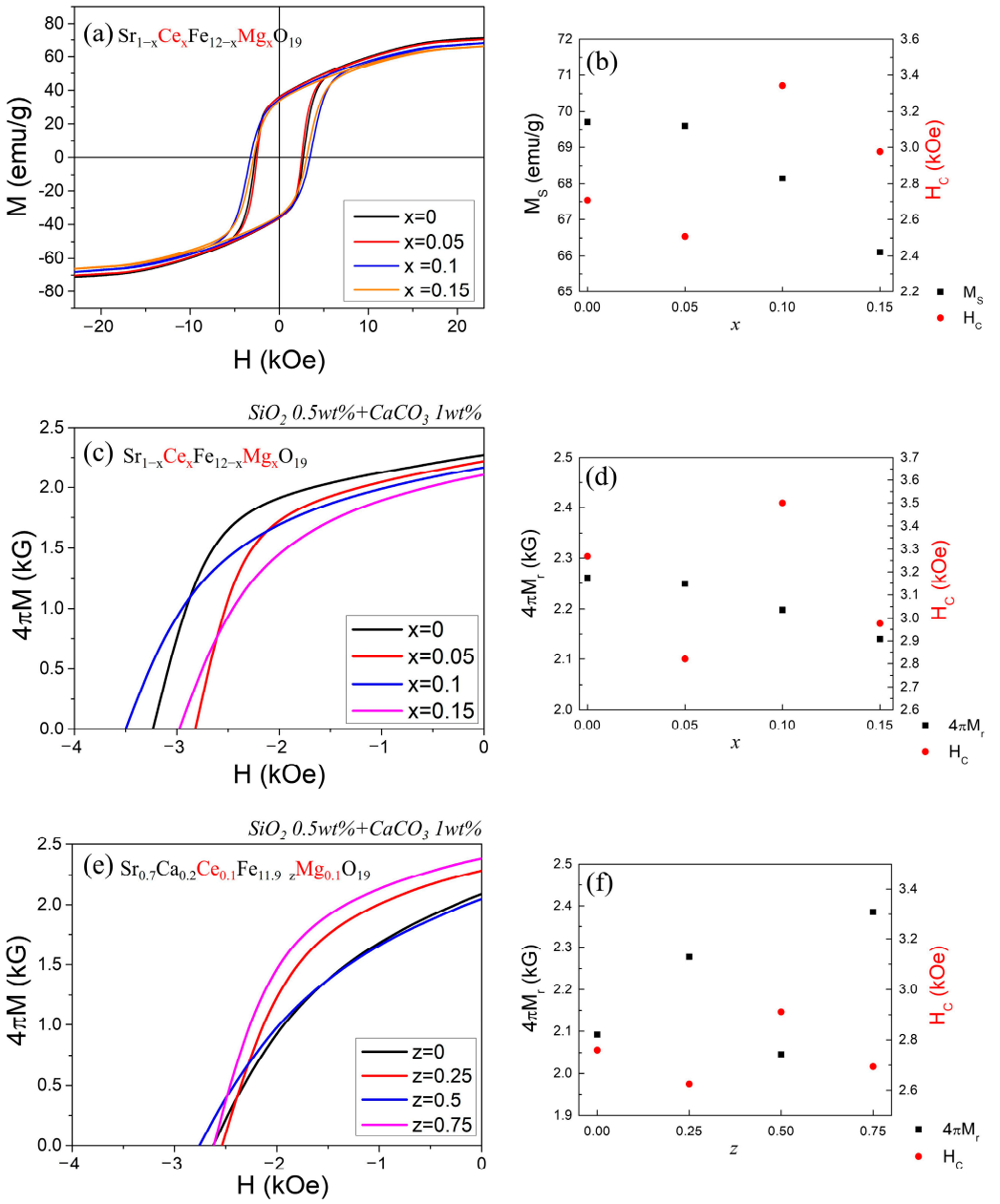


Figure 3. (**a**) VSM M–H curves and (**b**) corresponding M_S and H_C values versus x for $Sr_{1-x}Ce_xFe_{12-x}Mg_xO_{19}$; (**c**) B–H loop-tracer demagnetization curves and (**d**) corresponding $4\pi M_r$ and H_C values versus x for the same nominal compositions; (**e**) demagnetization curves and (**f**) corresponding $4\pi M_r$ and H_C values versus z for $Sr_{0.7}Ca_{0.2}Ce_{0.1}Fe_{11.9-z}Mg_{0.1}O_{19}$.

Notably, across the entire Ca-containing series ($Sr_{0.7}Ca_{0.2}Ce_{0.1}Fe_{11.9-z}Mg_{0.1}O_{19}$, z = 0–0.75), the H_C values (2760, 2625, 2911, and 2694 Oe at z = 0, 0.25, 0.5, and 0.75, respectively) remain distinctly lower than that of the Ca-free, x = 0.1 composition (3500 Oe, Figure 3c), and show no clear systematic dependence on z. The lower coercivity of the Ca-containing compositions may partly reflect grain coarsening during sintering, although contributions from changes in intrinsic anisotropy cannot be separated using the present measurements. This finding indicates that, once Ca is introduced to promote Ce incorporation, composition-specific control of the sintering temperature and sintering additives is required to counteract

Ca-induced grain coarsening and recover a fine coercivity-favorable microstructure—a requirement that is directly addressed in the sintering-additive optimization presented in the following section.

Table 2. Sample density, saturation magnetization (M_S) and coercivity (H_C) measured by VSM and remanent magnetization ($4\pi M_r$) and coercivity (H_C) measured by B–H loop tracer of the $Sr_{1-x}Ce_xFe_{12-x}Mg_xO_{19}$ (x = 0, 0.05, 0.1, 0.15) and $Sr_{0.7}Ca_{0.2}Ce_{0.1}Fe_{11.9-z}Mg_{0.1}O_{19}$ (z = 0, 0.25, 0.5, 0.75) powders after sintering at 1230 °C.

Composition	x or z	Density (g/cm^3)	VSM		B–H Loop Tracer	
			M_S (emu/g)	H_C (Oe)	$4\pi M_r$ (G)	H_C (Oe)
$Sr_{1-x}Ce_xFe_{12-x}Mg_xO_{19}$	0	4.78	69.71	2708	2261	3263
	0.05	4.84	69.60	2508	2249	2820
	0.1	4.62	68.15	3343	2198	3500
	0.15	4.67	66.11	2976	2140	2976
$Sr_{0.7}Ca_{0.2}Ce_{0.1}Fe_{11.9-z}Mg_{0.1}O_{19}$	0	4.77	-	-	2092	2760
	0.25	4.72	-	-	2277	2625
	0.50	4.76	-	-	2046	2911
	0.75	4.78	-	-	2385	2694

Estimated relative measurement errors are ≤0.4% for M_S and approximately 0.2% for $4\pi M_r$.

To address the grain coarsening and reduced coercivity observed in the Ca-containing compositions, the calcination temperature was lowered from 1100 to 1080 °C, and additional high-energy milling was introduced to refine the already-reacted powder. This approach aimed to facilitate densification at a lower sintering temperature while limiting grain growth. Figure 4a shows the $Sr_{0.7}Ca_{0.2}Ce_{0.1}Fe_{11.15}Mg_{0.1}O_{19}$ powder after 2 h of high-energy milling, immediately prior to sintering. The corresponding grain-size histogram (Figure 5a) confirms a fine and narrow starting particle size (D_{ave} = 0.70 μm), providing a common well-controlled starting point for all subsequent sintering trials. When this powder was sintered at 1210 °C without any additive (Figure 4b), pronounced grain growth occurred, with the average grain size increasing nearly threefold to D_{ave} = 2.02 μm (Figure 5b) and the distribution shifting to markedly larger sizes. The pronounced grain coarsening observed here is consistent with the reported grain-growth-promoting effect of Ca in related M-type ferrites [22,24] and may contribute to the lower coercivity of the Ca-containing compositions shown in Figure 3. Introducing sintering additives markedly curtailed this grain growth. Across all the additive combinations tested—SiO_2 + CaO (Figure 4c,d), SiO_2 + CaO + $SrCO_3$ (Figure 4e), and their further combinations with Cr_2O_3, ZnO, or Mn_2O_3 (Figure 4f–i)—the average grain size was reduced to a comparatively narrow range of D_{ave} = 1.12–1.43 μm (Figure 5c–i), roughly 30–45% smaller than the additive-free sample. The SiO_2/CaO-based additives suppressed grain coarsening under the present sintering conditions, possibly through reduced grain-boundary mobility associated with intergranular phases or solute-drag effects [17,24]. Notably, among the seven additive combinations examined, the resulting grain sizes and size distributions are all quite similar (D_{ave} = 1.12–1.43 μm), with no single combination producing a distinctly finer or more uniform microstructure than the others. This indicates that, once a baseline SiO_2/CaO addition is present to counteract Ca-induced grain growth, further variation in the minor additive components ($SrCO_3$, Cr_2O_3, ZnO, Mn_2O_3) has only a secondary relatively minor influence on the final grain structure—in contrast to the addition-versus-no-addition contrast, which is the dominant factor governing microstructural control in this system.

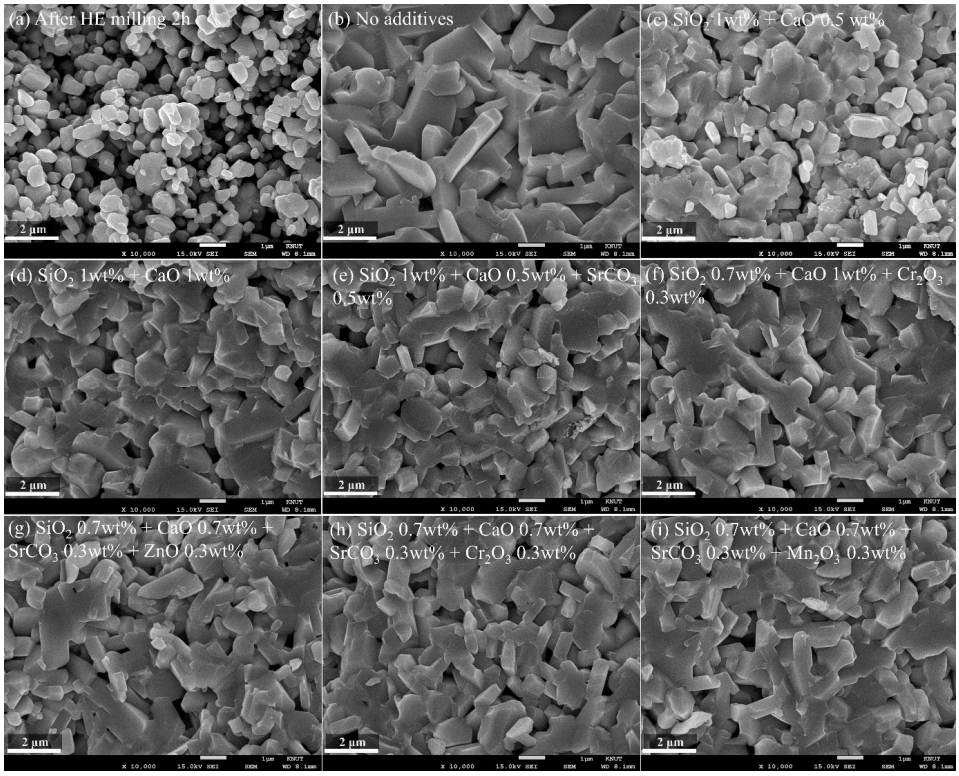


Figure 4. SEM micrographs of $Sr_{0.7}Ca_{0.2}Ce_{0.1}Fe_{11.15}Mg_{0.1}O_{19}$ (**a**) after high-energy milling for 2 h and (**b**–**i**) after sintering at 1210 °C for 2 h with various combinations of sintering additives.

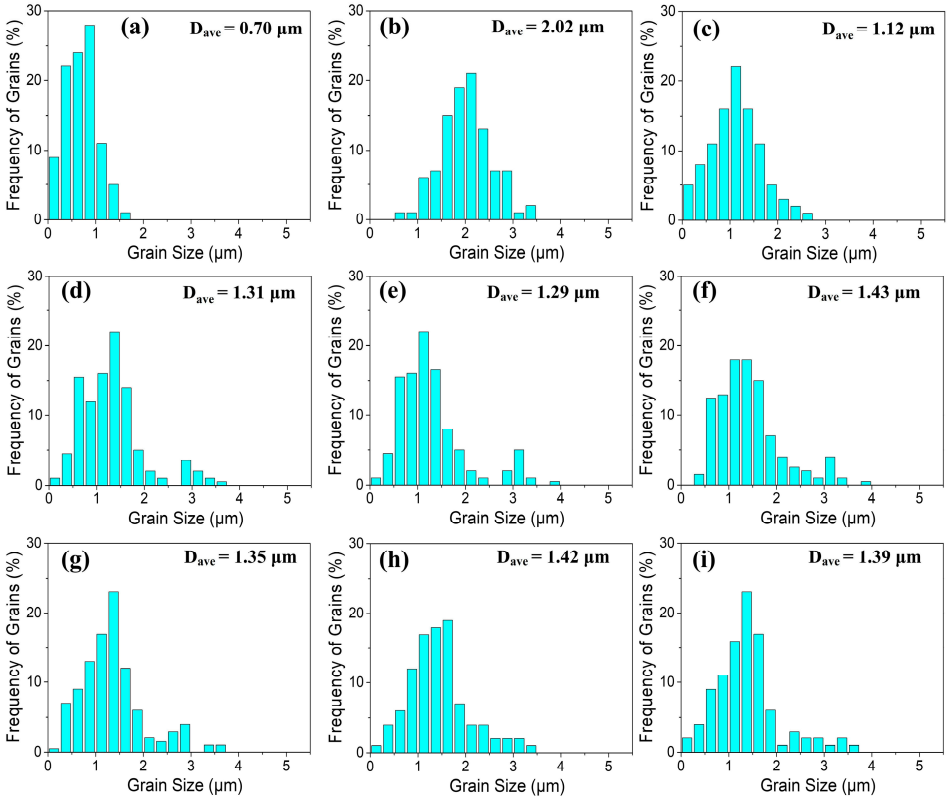


Figure 5. (**a**–**i**) Grain-size distribution histograms corresponding to the SEM micrographs of the $Sr_{0.7}Ca_{0.2}Ce_{0.1}Fe_{11.15}Mg_{0.1}O_{19}$ samples shown in Figure 4a–i.

Figure 6a compares the demagnetization curves of $Sr_{0.7}Ca_{0.2}Ce_{0.1}Fe_{11.15}Mg_{0.1}O_{19}$ (with the SiO_2/CaO-based additive package) sintered at 1210, 1220, and 1230 °C. Unlike the composition examined in Figure 3, which was not subjected to the additional high-energy milling step, this final composition shows a marked sensitivity to sintering temperature once high-energy milling is applied. At 1230 °C, pronounced grain growth severely degrades the loop squareness and sharply reduces H_C; at 1220 °C, the curve remains distinctly non-square, indicating that some coarse grains persist even at this intermediate temperature. Only at 1210 °C is a well-squared demagnetization curve obtained, reflecting a fine growth-controlled grain structure.

Accordingly, 1210 °C was selected for the subsequent additive trials, indicating that the modified powder-processing route enabled sintering at a temperature 20 °C below the initial 1230 °C condition while retaining a favorable demagnetization-curve shape. The density and magnetic properties of the sintered samples with different additives (O, A–G) are presented in Table 3. Figure 6b and the accompanying data table compare the additive-free sample (O) with seven additive combinations (A–G), all sintered at 1210 °C. The additive-free sample O exhibits a comparatively low H_C of 2714 Oe, consistent with the coarse grain structure observed for the additive-free condition in Figure 4b/Figure 5b (D_{ave} = 2.02 μm). Introducing any additive combination raises H_C substantially, to 3552–3911 Oe, alongside the grain refinement observed in Figure 5c–i (D_{ave} = 1.12–1.43 μm), consistent with grain refinement contributing to the coercivity enhancement.

Among the additive combinations, sample A (SiO_2 1 wt % + CaO 0.5 wt %) gives the highest H_C (3911 Oe), while the remaining combinations (B, C, D, F, G), which additionally include $SrCO_3$, Cr_2O_3, and/or Mn_2O_3, show comparably high H_C (3648–3741 Oe) without a clear further improvement over the simplest SiO_2/CaO base—consistent with the similarly narrow grain-size range found for these samples in Figure 5. Sample E (SiO_2 0.7 + CaO 0.7 + $SrCO_3$ 0.3 + ZnO 0.3 wt %) stands out from this trend: despite a grain size comparable to the other additive-containing samples (Figure 5), it shows the lowest H_C among all additive samples (3552 Oe) together with the highest $4\pi M_r$ among them (2328 G), and indeed the second-highest $4\pi M_r$ of the entire series after the coarse-grained sample O (2368 G). The relatively high $4\pi M_r$ and lower H_C of sample E, despite its grain size being comparable to those of the other additive-containing samples, may be associated with the known preference of Zn^{2+} for spin-down Fe^{3+} sites [25]. Such substitution could increase the net magnetization while modifying magnetic interactions and reducing coercivity. The comparable density of sample E (4.80 g/cm^3) suggests that further densification is unlikely to be the main cause.

Table 3. Sample density, remanent magnetization ($4\pi M_r$) and coercivity (H_C) measured by B–H loop tracer of the $Sr_{0.7}Ca_{0.2}Ce_{0.1}Fe_{11.15}Mg_{0.1}O_{19}$ sintered at 1210 °C for 2 h with various combinations of additives.

Additives (wt %)	Density (g/cm^3)	BH-Tracer	
		$4\pi M_r$ (G)	H_C (Oe)
(O) No additives	4.75	2368	2714
(A) SiO_2 1 wt % + CaO 0.5 wt %	4.69	2183	3911
(B) SiO_2 1 wt % + CaO 1 wt %	4.72	2284	3729
(C) SiO_2 1 wt % + CaO 0.5 wt % + $SrCO_3$ 0.5 wt %	4.82	2298	3741
(D) SiO_2 0.7 wt % + CaO 1 wt % + Cr_2O_3 0.3 wt %	4.79	2229	3690
(E) SiO_2 0.7 wt % + CaO 0.7 wt % + $SrCO_3$ 0.3 wt % + ZnO 0.3wt %	4.80	2328	3552
(F) SiO_2 0.7 wt % + CaO 0.7 wt % + $SrCO_3$ 0.3wt % + Cr_2O_3 0.3wt %	4.76	2307	3691
(G) SiO_2 0.7 wt % + CaO 0.7 wt % + $SrCO_3$ 0.3wt % + Mn_2O_3 0.3wt %	4.80	2276	3648

The estimated relative measurement error in $4\pi M_r$ is approximately 0.2%.

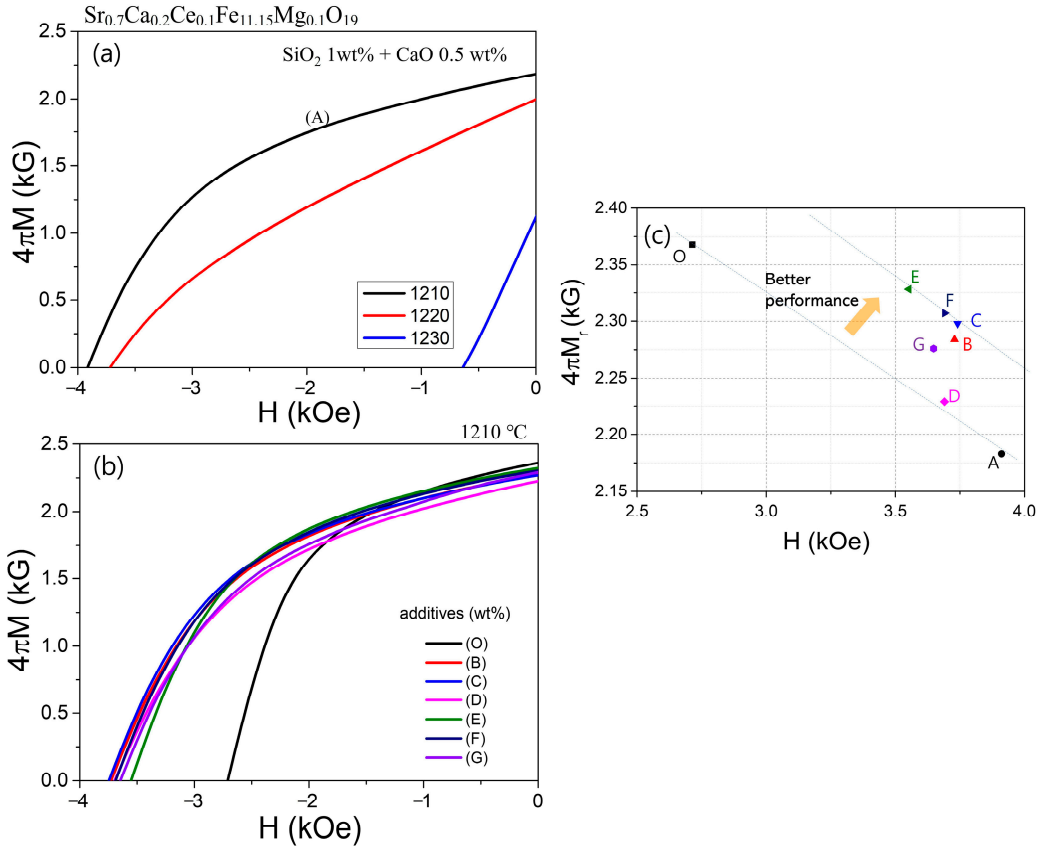


Figure 6. (**a**) Demagnetization curves (4πM vs. H) of $Sr_{0.7}Ca_{0.2}Ce_{0.1}Fe_{11.15}Mg_{0.1}O_{19}$ samples sintered at 1210, 1220, and 1230 °C; (**b**) demagnetization curves of $Sr_{0.7}Ca_{0.2}Ce_{0.1}Fe_{11.15}Mg_{0.1}O_{19}$ samples sintered at 1210 °C with various combinations of sintering additives; and (**c**) plot of remanent magnetization ($4\pi M_r$) versus coercivity (H_C) for all samples. Sample labels O and A–G correspond to the additive formulations listed in Table 3.

These trade-offs are summarized in Figure 6c, a $4\pi M_r$–H_C plot of all samples. Sample O occupies the high-$4\pi M_r$/low-H_C corner, while the additive-containing samples (A–G) shift markedly toward higher H_C, with sample A reaching the highest H_C and sample E standing apart by combining a high H_C gain with an elevated $4\pi M_r$, making it the most balanced composition among the additive series. This progression—from enhancing Ce incorporation, as suggested by the suppression of CeO_2 reflections (Figure 1) and nominal Fe-content adjustment (Figure 1c, Figure 3e), through microstructural control via high-energy milling and sintering-temperature optimization, to fine-tuning the $4\pi M_r$–H_C balance via sintering additives (Figures 4–6)—demonstrates a systematic composition- and process-driven pathway for maximizing the hard magnetic performance of a Ca–Ce–Mg co-substituted, cobalt-free M-type hexaferrite. The resulting H_C and $4\pi M_r$ values do not surpass those reported for high-performance La–Co-substituted ferrites. However, the present specimens were prepared without magnetic-field alignment. Comparisons with field-aligned or commercial anisotropic ferrites should therefore account for differences in orientation, density, and processing, particularly when evaluating remanence and maximum energy product ($(BH)_{max}$). These results provide a compositional and processing basis for further development of Co-free ferrite magnets [26].

4. Summary

Ce–Mg co-substituted M-type hexaferrites were developed to resolve the coupled compositional and processing challenges of incorporating cerium into the $SrFe_{12}O_{19}$ lattice. In

$Sr_{1-x}Ce_xFe_{12-x}Mg_xO_{19}$ (x = 0–0.15), a residual CeO_2 phase persisted at every composition, suggesting limited Ce incorporation under the present processing conditions, although x = 0.1 gave the finest grain structure and highest coercivity. Partial substitution of Ca^{2+} for Sr^{2+} suppressed detectable CeO_2 reflections at y ≥ 0.2 in $Sr_{0.9-y}Ca_yCe_{0.1}Fe_{11.9}Mg_{0.1}O_{19}$, providing indirect evidence for enhanced Ce incorporation, although an α-Fe_2O_3 secondary phase remained. Reducing the nominal Fe content in $Sr_{0.7}Ca_{0.2}Ce_{0.1}Fe_{11.9-z}Mg_{0.1}O_{19}$ (z = 0–0.75) suppressed this secondary phase, with no detectable α- Fe_2O_3 reflection at z = 0.75 ($Sr_{0.7}Ca_{0.2}Ce_{0.1}Fe_{11.15}Mg_{0.1}O_{19}$). Because Ca^{2+} also promoted grain growth and lowered coercivity, high-energy milling combined with sintering-temperature and additive optimization (SiO_2, CaO, $SrCO_3$, Cr_2O_3, ZnO, Mn_2O_3) was applied, raising the coercivity from 2714 Oe (additive-free) to 3552–3911 Oe at 1210 °C. Sample A (SiO_2/CaO) gave the highest coercivity (3911 Oe) but the lowest remanence, illustrating the typical $4\pi M_r$–H_C trade-off. In contrast, the $SrCO_3$-based combinations E, F, and G (with ZnO, Cr_2O_3, or Mn_2O_3, respectively) achieved a closely matched and favorably balanced performance ($4\pi M_r$ = 2276–2328 G, H_C = 3552–3691 Oe), with sample E showing the highest measured remanence among the additive-containing specimens, possibly associated with Zn-related changes in sublattice magnetism beyond grain-size effects alone. These results demonstrate a Co-free composition–processing route combining Ca-assisted Ce incorporation, nominal Fe-content adjustment, and grain-size control to tailor the hard magnetic properties of Ce-substituted M-type hexaferrites, providing a basis for further magnet development. Future work will include independently prepared replicate batches and statistical analysis of magnetic properties to establish reproducibility and assess the significance of differences among closely performing compositions.

Author Contributions: Conceptualization, Y.-M.K.; methodology, D.-H.K.; software, D.-H.K.; validation, Y.-M.K. and D.-H.K.; formal analysis, Y.-M.K. and D.-H.K.; investigation, Y.-M.K. and D.-H.K.; writing—original draft preparation, Y.-M.K.; writing—review and editing, Y.-M.K.; visualization, Y.-M.K. and D.-H.K.; supervision, Y.-M.K.; project administration, Y.-M.K.; funding acquisition, Y.-M.K. All authors have read and agreed to the published version of the manuscript.

Funding: This work was supported by National Research Foundation of Korea (NRF) grants funded by the Korean Government (MSIT) (RS-2026-25604779).

Institutional Review Board Statement: Not applicable.

Informed Consent Statement: Not applicable.

Data Availability Statement: The numerical data supporting the findings of this study are available from the corresponding author upon reasonable request.

Conflicts of Interest: The authors declare no conflicts of interest.

References

1. Went, J.J.; Rathenau, G.W.; Gorter, E.W.; Van Oosterhout, G.W. Ferroxdure. A Class of Permanent Magnetic Materials. *Philips Tech. Rev.* **1952**, *13*, 194–208.
2. Smit, J.; Wijn, H.P.J. *Ferrites: Physical Properties of Ferromagnetic Oxides in Relation to Their Technical Applications*; Philips Technical Library: Eindhoven, The Netherlands, 1959.
3. Taguchi, H. Recent improvements of ferrite magnets. *J. Phys. IV Fr.* **1997**, *7*, C1-299–C1-302. [CrossRef]
4. Pullar, R.C. Hexagonal ferrites: A review of the synthesis, properties and applications of hexaferrite ceramics. *Prog. Mater. Sci.* **2012**, *57*, 1191–1334. [CrossRef]
5. de Julián Fernández, C.; Sangregorio, C.; de la Figuera, J.; Belec, B.; Makovec, D.; Quesada, A. Progress and prospects of hard hexaferrites for permanent magnet applications. *J. Phys. D Appl. Phys.* **2021**, *54*, 153001. [CrossRef]
6. Sudakar, C.; Subbanna, G.N.; Kutty, T.R.N. Wet chemical synthesis of multicomponent hexaferrites by gel-to-crystallite conversion and their magnetic properties. *J. Magn. Magn. Mater.* **2003**, *263*, 253–268. [CrossRef]

7. Kools, F.; Morel, A.; Grössinger, R.; Le Breton, J.M.; Tenaud, P. LaCo-substituted ferrite magnets, a new class of high-grade ceramic magnets; intrinsic and microstructural aspects. *J. Magn. Magn. Mater.* **2002**, *242–245*, 1270–1276. [CrossRef]
8. Ogata, Y.; Takami, T.; Kubota, Y. Development of La-Co substituted ferrite magnets. *J. Jpn. Soc. Powder Metall.* **2003**, *50*, 636–641. [CrossRef]
9. Kobayashi, Y.; Hosokawa, S.; Oda, E.; Toyota, S. Magnetic properties and composition of Ca-La-Co M-type ferrites. *J. Jpn. Soc. Powder Metall.* **2008**, *55*, 541–546. [CrossRef]
10. Grossinger, R.; Kupferling, M.; Blanco, J.C.T.; Wiesinger, G.; Muller, M.; Hilscher, G.; Pieper, M.W.; Wang, J.F.; Harris, I. Rare earth substitutions in M-type ferrites. *IEEE Trans. Magn.* **2003**, *39*, 2911–2913. [CrossRef]
11. Lobo-Guerrero, A.; Salazar-Muñoz, V.E.; Aguilera Del Toro, R.H.; Hernández-Vázquez, E.E. M-type hexaferrites: A review of the impact of rare earth substitution on magnetic properties. *J. Magn. Magn. Mater.* **2025**, *627*, 173132. [CrossRef]
12. Todkar, G.B.; Kunale, R.A.; Kamble, R.N.; Batoo, K.M.; Ijaz, M.F.; Imran, A.; Hadi, M.; Raslan, E.H.; Shirsath, S.E.; Kadam, R.H. Ce–Dy substituted barium hexaferrite nanoparticles with large coercivity for permanent magnet and microwave absorber application. *J. Phys. D Appl. Phys.* **2021**, *54*, 294001. [CrossRef]
13. Kang, Y.-M.; Moon, K.-S. Magnetic properties of Ce–Mn substituted M-type Sr-hexaferrites. *Ceram. Int.* **2015**, *41*, 12828–12834. [CrossRef]
14. Kang, Y.-M. High saturation magnetization in La–Ce–Zn–doped M-type Sr-hexaferrites. *Ceram. Int.* **2015**, *41*, 4354–4359. [CrossRef]
15. Waki, T.; Nakai, S.; Tabata, Y.; Nakamura, H. Role of oxygen potential in dopant solubility in ferrite magnets: Enhanced Zn solubility and magnetization in La–Zn co-substituted magnetoplumbite-type strontium ferrite. *Mater. Res. Bull.* **2023**, *168*, 112470. [CrossRef]
16. Tanwar, K.; Gyan, D.S.; Gupta, P.; Pandey, S.; OmParkash; Kumar, D. Investigation of crystal structure, microstructure and low temperature magnetic behavior of Ce^{4+} and Zn^{2+} co-doped barium hexaferrites ($BaFe_{12}O_{19}$). *RSC Adv.* **2018**, *8*, 19600–19609. [CrossRef] [PubMed]
17. Kim, J.-J.; Kang, Y.-M. La–Mg-Substituted M-Type Sr-Hexaferrites for Enhanced Hard Magnetic Properties. *Appl. Sci.* **2025**, *15*, 11764. [CrossRef]
18. Cao, C.; Li, X.; Luo, B.; Li, Y.; Zhang, A.; Xia, A. Ce-substituted M-type $SrFe_{12}O_{19}$ ferrites: Phase formation and magnetic properties. *J. Supercond. Nov. Magn.* **2018**, *31*, 1247–1251. [CrossRef]
19. Lim, J.-P.; Kang, M.-G.; Kang, Y.-M. Development of multi-cation-doped M-type hexaferrite permanent magnets. *Appl. Sci.* **2023**, *13*, 295. [CrossRef]
20. Lee, J.; Lee, E.J.; Hwang, T.-Y.; Kim, J.; Choa, Y.-H. Anisotropic characteristics and improved magnetic performance of Ca–La–Co-substituted strontium hexaferrite nanomagnets. *Sci. Rep.* **2020**, *10*, 15929. [CrossRef] [PubMed]
21. Nakamura, H.; Ohta, H.; Kobayashi, R.; Waki, T.; Tabata, Y.; Ikeno, H.; Mény, C. Site-selective cobalt substitution in La–Co co-substituted magnetoplumbite-type ferrites: ^{59}Co-NMR and DFT calculation study. *J. Phys. Mater.* **2024**, *7*, 025012. [CrossRef]
22. Moon, K.-S.; Lim, E.-S.; Kang, Y.-M. Effect of Ca and La substitution on the structure and magnetic properties of M-type Sr-hexaferrites. *J. Alloys Compd.* **2019**, *771*, 350–355. [CrossRef]
23. Nishio, H.; Minachi, Y.; Yamamoto, H. Effect of factors on coercivity in Sr-La-Co sintered ferrite magnets. *IEEE Trans. Magn.* **2009**, *45*, 5281–5288. [CrossRef]
24. Topfer, J.; Schwarzer, S.; Senz, S.; Hesse, D. Influence of SiO_2 and CaO additions on the microstructure and magnetic properties of sintered Sr-hexaferrite. *J. Eur. Ceram. Soc.* **2005**, *25*, 1681–1688. [CrossRef]
25. Dixit, V.; Thapa, D.; Lamichhane, B.; Nandadasa, C.N.; Hong, Y.-K.; Kim, S.-G. Site preference and magnetic properties of Zn-Sn-substituted strontium hexaferrite. *J. Appl. Phys.* **2019**, *125*, 173901. [CrossRef]
26. Valentin, J.L.; Gjørup, F.H.; Knudsen, C.G.; Christensen, M. Grain alignment in hexaferrite permanent magnets by compaction at room and elevated temperatures. *Nanoscale* **2024**, *16*, 21106–21117. [CrossRef] [PubMed]

Disclaimer/Publisher's Note: The statements, opinions and data contained in all publications are solely those of the individual author(s) and contributor(s) and not of MDPI and/or the editor(s). MDPI and/or the editor(s) disclaim responsibility for any injury to people or property resulting from any ideas, methods, instructions or products referred to in the content.